Effects of weakly coupled channels on quasielastic barrier distributions

E. Piasecki,[1,2] Ł. Świderski,[2] W. Gawlikowicz,[1] J. Jastrzębski,[1] N. Keeley,[2] M. Kisieliński,[1,2] S. Kliczewski,[3] A. Kordyasz,[1] M. Kowalczyk,[1,4] S. Khlebnikov,[5] E. Koshchiy,[6] E. Kozulin,[7] T. Krogulski,[8] T. Loktev,[7] M. Mutterer,[9] K. Piasecki,[4] A. Piórkowska,[10] K. Rusek,[2] A. Staudt,[10] M. Sillanpää,[11] S. Smirnov,[7] I. Strojek,[2] G. Tiourin,[11] W. H. Trzaska,[11] A. Trzcińska,[1] K. Hagino,[12] and N. Rowley[13,*]

[1]*Heavy Ion Laboratory, Warsaw University, Warsaw, Poland*
[2]*The Andrzej Sołtan Institute for Nuclear Studies, Świerk, Poland*
[3]*The Henryk Niewodniczański Institute of Nuclear Physics, Kraków, Poland*
[4]*Institute of Experimental Physics, Warsaw University, Warsaw, Poland*
[5]*Khloplin Radium Institute, St. Petersburg, Russia*
[6]*Kharkiv University, Kharkiv, Ukraine*
[7]*JINR, Dubna, Russia*
[8]*Faculty of Physics, University of Białystok, Białystok, Poland*
[9]*Institut für Kernphysik, Technische Universität Darmstadt, Darmstadt, Germany*
[10]*Institute of Physics, University of Silesia, Katowice, Poland*
[11]*Department of Physics, University of Jyväskylä, Jyväskylä, Finland*
[12]*Department of Physics, Tohoku University, Sendai 980-8578, Japan*
[13]*Institut de Physique Nucléaire, UMR 8608, CNRS-IN2P3 et Université de Paris Sud, 91406 Orsay Cedex, France*

(Received 24 January 2009; revised manuscript received 29 September 2009; published 25 November 2009)

Heavy-ion collisions often produce fusion barrier distributions with structures displaying a fingerprint of couplings to highly collective excitations. Similar distributions can be obtained from large-angle quasielastic scattering, although in this case, the role of the many weak direct-reaction channels is unclear. For ^{20}Ne + ^{90}Zr, we have observed the barrier structures expected for the highly deformed neon projectile; however, for ^{20}Ne + ^{92}Zr, we find significant extra absorption into a large number of noncollective inelastic channels. This leads to smearing of the barrier distribution and a consequent reduction in the "resolving power" of the quasielastic method.

DOI: 10.1103/PhysRevC.80.054613 PACS number(s): 25.70.Jj, 24.10.Eq, 25.70.Bc, 25.70.Hi

I. INTRODUCTION

Nuclear reactions at sub-barrier energies play an extremely important role in nature, being responsible for the fundamental behavior of stars, their evolution, and many aspects of the creation of the elements. One of the most important near-barrier reactions is fusion. It is well known that the interplay between the relative motion of two colliding nuclei and their internal structures can manifest itself in a strong enhancement of fusion cross sections at sub-barrier energies [1]. Such effects have important analogs in other branches of physics and chemistry and belong to the general phenomenon known as "tunneling in the presence of an environment" [2]. For many nuclear systems, experiments show that coupling to highly collective states leads to a distribution of Coulomb barrier heights, which can be determined directly [3] from the fusion excitation function $\sigma_{\rm fus}(E)$ or from backscattered quasielastic events [4–6] [see Eqs. (2) and (3)].

The latter method consists of determining the quasielastic (QE) excitation function $\sigma_{\rm QE}(E,\theta)$ for projectile-like nuclei at large center-of-mass (CM) scattering angles θ, that is, the sum of elastic, inelastic, and transfer channels, with, in principle, no need to distinguish the particular channels involved. The barrier distribution is obtained directly from the data as the first derivative of $\sigma_{\rm QE}$ divided by the Rutherford cross section σ_R [see Eq. (3)]. The measurements consist simply of counting the number of projectile-like nuclei registered at backward and forward angles, the latter giving a measure of σ_R. These approaches usually give very similar results, although at least one experimental example of a discrepancy (in the ^{16}O + ^{144}Sm system) has been found [4,7].

In a recent paper [8], Zagrebaev remarked that the QE method determines a threshold distribution for all reaction processes rather than just for fusion and that this has important implications in the case of very heavy systems, where contributions from deep-inelastic collisions are important. Here, however, we concentrate on systems where these processes are negligible.

The QE method has a minor complication relative to fusion measurements; that is, the excitation function depends on the angle θ at which the measurement is made. This is simply due to the extra centrifugal potential for the partial waves contributing to the scattering at θ. This can, however, be advantageous because measurements at an angle θ can be transformed to measurements at 180° at an "effective energy" [9]

$$E_{\rm eff} = \frac{2E}{1+\mathrm{cosec}(\theta/2)}. \quad (1)$$

Thus, several effective energies can be measured simultaneously for a single incident energy by using detectors at different, large angles.

[*]On *mise à disposition* at the STFC Daresbury Laboratory, Warrington WA4 4AD, United Kingdom.

In many cases, the barrier distributions turn out to be markedly structured (multipeaked), giving a fingerprint of the strong couplings involved. For fusion at a CM energy E, we may consider the distribution to be given by a weighted sum over different barriers i having weights w_i and heights B_i:

$$D_{\rm fus}(E) \equiv \frac{1}{\pi R^2}\frac{d^2(E\sigma_{\rm fus})}{dE^2} \approx \sum_i w_i f_{\rm fus}(E-B_i) \equiv \sum_i w_i \left[\frac{1}{\pi R^2}\frac{d^2(E\sigma_{\rm fus})}{dE^2}\right]_i, \quad (2)$$

where $\sum_i w_i = 1$. Here, R is the average barrier radius, and the fusion "test functions" $f_{\rm fus}(E-B_i)$ (i.e., simply the individual peaks corresponding to each barrier) are evaluated for single (uncoupled) barriers of height B_i. The summation in this equation can be best understood for deformed nuclei, where, classically, the different barriers arise from different orientations of the target, and the sum is simply the quantum mechanical analog of the integral over all possible orientations [10].

For the quasielastic process, we may similarly define

$$D_{\rm QE}(E_{\rm eff}) \equiv -\frac{d(\sigma_{\rm QE}/\sigma_R)}{dE_{\rm eff}} \approx \sum_i w_i f_{\rm QE}(E_{\rm eff}-B_i) \equiv \sum_i w_i \left[-\frac{d(\sigma_{\rm QE}/\sigma_R)}{dE_{\rm eff}}\right]_i, \quad (3)$$

generated by the *same* set of uncoupled barriers [6]. As with Eq. (2), this expression is rather simple, because all of the test functions $f_{\rm QE}(E-B_i)$ have the same shape, but merely peak at different values of B_i. To see the barrier structures clearly, adjacent test functions must be sufficiently narrow relative to their separations; otherwise they will overlap and the resulting total barrier distribution will become smooth.

Theoretically, one can use the coupled-channel (CC) approach to account explicitly for the strong, collective excitations and demonstrate the basic equivalence of the described quantities [1,6]. However, the role of the weaker, direct-reaction channels is less clear, and their inclusion in a CC scheme is usually impossible owing to their large number and the complexity of their couplings. The principal object of this paper is to investigate the role of weakly coupled channels in quasielastic scattering. We shall see that the new effects that they introduce limit the capability of quasielastic experiments to resolve the barrier structures that contain the information on the nuclear-reaction dynamics.

II. EXPERIMENTAL RESULTS

A. Quasielastic scattering of ^{20}Ne

Our program of measurements has concentrated on the ^{20}Ne projectile, because this nucleus has spectacularly large deformation parameters—$\beta_2 = 0.46$, $\beta_3 = 0.39$, and $\beta_4 = 0.27$ [11]—and, in many cases, this should completely dominate the barrier structures. We propose here to study quasielastic scattering in the systems ^{20}Ne + ^{90,92}Zr. Calculations show that $D_{\rm QE}$ should essentially be the same in both reactions. This provides, therefore, an excellent opportunity for studying the role of differences due to the weaker direct-reaction channels, expected to be much less important in the closed neutron shell ^{90}Zr nucleus.

The method and experimental setup, as well as the data analysis, are described in Refs. [12,13]. Briefly, we measured the QE large-angle scattering using 30 10×10 mm PIN diodes placed 9 cm from the target at 130°, 140°, and 150° in the laboratory system and two "Rutherford" semiconductor detectors (6 mm diameter) placed at a distance of 27 cm at 35° with respect to the beam. The ^{20}Ne beam, with an intensity of a few particle-nanoamperes (pnA) from the Warsaw Cyclotron, bombarded 100 μg/cm^2 targets of ^{90}Zr and ^{92}Zr (enriched to 98%) on 20 μg/cm^2 C backings, produced at the Legnaro National Laboratory. The use of nickel foils as energy degraders and measurements at the described angles leads to an excitation function with small effective-energy intervals (see Fig. 1). Energy calibration was performed using a precise pulse generator and Bi-Po α-particle sources (the estimated pulse-height defect of the semiconductor detectors being negligibly small). Energy resolution was continuously monitored during the experiment using the energy spectra measured in the forward detectors, and turned out to be about 1.2 MeV full width half maximum (FWHM) for both targets. Apart from contributions coming from straggling in the degrader and the energy loss in the target (about 0.3 MeV each), the main contribution to the width comes from characteristics of the beam. Other effects, for example, the geometry of detection, had very little influence on the energy resolution. The resolution and stability of the electronics and detectors were continuously monitored using a pulse generator and an α-particle source.

From the kinetic-energy spectra, assuming two-body kinematics, we calculated the Q-value spectra for the forward and backward detectors. Then, by integration, the number

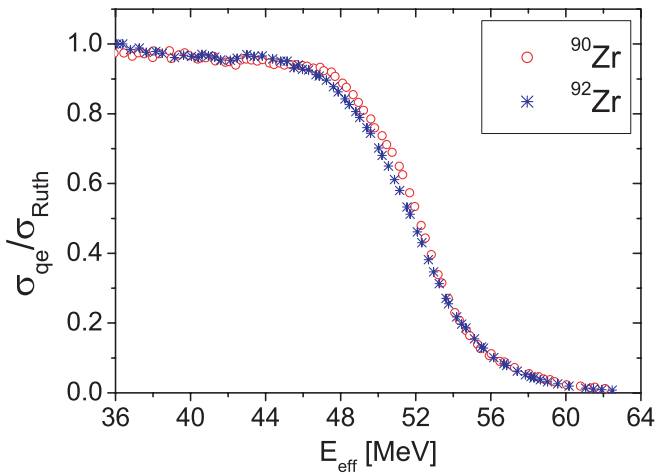

FIG. 1. (Color online) Comparison of the excitation functions for backscattering of ^{20}Ne on ^{90,92}Zr isotopes.

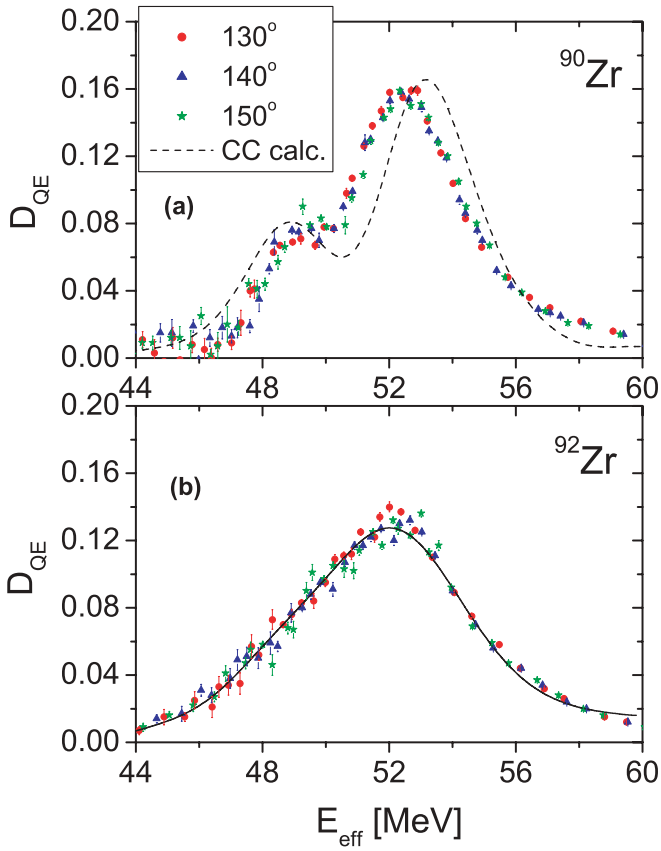

FIG. 2. (Color online) Barrier distributions for the ^{20}Ne + ^{90,92}Zr systems [panels (a) and (b), respectively]. Different symbols refer to different laboratory detector angles. The scaling to $E_{\rm eff}$ (see text) can be seen to be very good. The dashed line in the upper panel shows the CC prediction [folded with the experimental resolution of 1.2 MeV (FWHM)]. The solid line in the lower panel shows the result of transforming the ^{20}Ne + ^{90}Zr experimental data as described in the text (see Sec. III). This transformation reproduces extremely well the ^{20}Ne + ^{92}Zr data, without any input from the CC calculations.

of counts was obtained. The effective energy was calculated and, after binning the data over 0.3-MeV intervals, the corresponding $\sigma_{\rm QE}/\sigma_R$ was constructed (see Fig. 1). Then, the barrier distributions of Figs. 2(a) and 2(b) were determined using the finite-difference method. The results confirm those of Ref. [12], but with significantly better statistics.

The results of calculations performed with the code CCQUEL [14] are shown in Fig. 2(a) for ^{20}Ne + ^{90}Zr. They include couplings between the 0^+, 2^+, 4^+, and 6^+ states in the ^{20}Ne rotational band. The results converge rapidly as the number of states is increased, and it was verified that truncating the calculations at the 4^+ level is entirely sufficient for our purposes. We also took account of the strong octupole-phonon state of the projectile and the vibrational excitations of the target. However, because the ^{90}Zr deformation parameters are small compared with those for ^{20}Ne, they have a practically negligible effect on the barrier distribution (see also Fig. 5). For the same reason, the calculated distribution for ^{20}Ne + ^{92}Zr is almost identical to that for ^{20}Ne + ^{90}Zr and is not shown.

The calculations reproduce a structure very similar to that seen in the data for ^{20}Ne + ^{90}Zr. More important, though, is the clear difference between the *measured* distributions for the ^{90}Zr and the ^{92}Zr targets: Whereas the former displays this well-defined structure, the latter is virtually structureless and wider, in conflict with the theoretical calculations.

Although the correct shape is reproduced, the theoretical barrier distribution for ^{20}Ne + ^{90}Zr is clearly wider than the experimental one, and this is almost certainly due to an approximation made in the CC calculations. That is, the nucleus-nucleus potential is a function of the distance between the nuclear surfaces along the line joining their centers. For the extreme deformations that we have here, it is more correct to use the minimum (perpendicular) distance between the surfaces [15]. This will be investigated elsewhere, but it is not important for our current considerations, since we shall show in Sec. III how the data for ^{20}Ne + ^{92}Zr can be reproduced by a direct transformation of the experimental data for the ^{20}Ne + ^{90}Zr system. The transformed ^{20}Ne + ^{90}Zr data are shown as the solid curve in the lower part of the figure and are seen to fit those for ^{20}Ne + ^{92}Zr extremely well. We shall see that this transformation is related simply to the optical-model potential that describes absorption into the weak, inelastic channels in the ^{20}Ne + ^{92}Zr reaction.

B. Role of transfer channels

In certain cases, transfer channels have been suggested as the reason for discrepancies between measured and calculated $D_{\rm fus}$. A well-studied example is the reactions ^{40}Ca + ^{90,96}Zr, where clear differences between $D_{\rm fus}$ exist (structured for ^{90}Zr and smooth for the ^{96}Zr target), and there has been some debate over whether neutron-transfer channels might be responsible for smoothing the ^{40}Ca + ^{96}Zr distribution [9,16,17]. Although these transfers are significantly stronger for ^{40}Ca + ^{96}Zr, the effect of the ^{96}Zr octupole phonon appears to play the dominant role in this system owing to the spherical, doubly magic nature of the projectile. However, for our systems, any differences in the target-phonon structures are swamped by the projectile deformation, and the only possible explanation of the observed, strong isotopic effect is differences in the weak, direct-reaction channels, in principle, including both transfers and noncollective inelastic excitations.

According to their Q values, the transfer probability for ^{20}Ne + ^{92}Zr should be much larger than that for ^{20}Ne + ^{90}Zr. To check this, a separate experiment was performed, in which transfer cross sections were directly measured for both systems at a CM angle around 156° and at the energy corresponding to the secondary hump seen for the ^{90}Zr target (at $E_{\rm eff} \approx$ 50 MeV).

The time-of-flight (TOF) technique was used to identify the masses of backscattered ions. The scheme of the experimental setup is presented in Fig. 3. The "start" signal was given by the microchannel-plate (MCP) detector. The "stop" signal was triggered by an array of four 20 × 20 mm semiconductor detectors, placed at a CM angle around 156°. The flight base of 750 mm and time resolution of ∼250 ps resulted in a good mass resolution of ∼0.14 amu (FWHM). Three ancillary

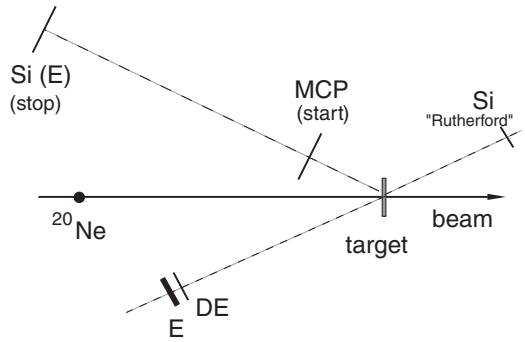

FIG. 3. Schematic view of the measurement setup (see detailed description in the text).

detectors were employed simultaneously: The isobutane-filled ΔE detector telescope ensured a low energy threshold and perfect identification of all registered ion charges, and two silicon (Rutherford) detectors placed at forward angles of 38° (in the laboratory system) were used to monitor the beam energy. The data analysis gave us production probabilities for ions of masses in the range $A = 12$–22. The main results are presented in Fig. 4. These complement and constitute an improvement on the earlier results of Ref. [18].

The most striking result is that the total transfer cross sections for the ^{90}Zr and ^{92}Zr targets are essentially the same, namely, 3.46(17) and 3.74(19) mb/ster, respectively (just 6% of the total quasielastic scattering at this angle). This equality implies that while transfers can, in principle, play a significant role in the shape of barrier distributions (see, e.g., Ref. [19]), some other mechanism is responsible for the very marked difference between the barrier distributions for the two zirconium isotopes.

The most likely explanation can be seen in Fig. 5, where we compare the Q-value spectra for (nontransfer) backscattered

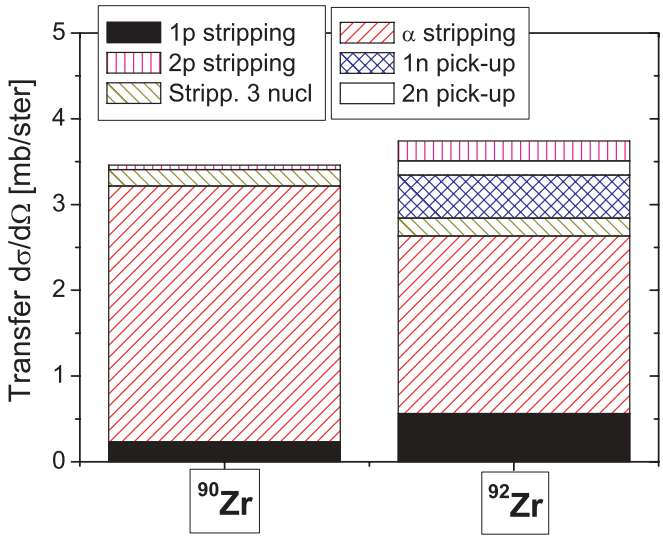

FIG. 4. (Color online) Comparison of differential transfer cross sections measured for the ^{20}Ne + ^{90,92}Zr systems at $E_{\text{eff}} = 50$ MeV and a CM angle around 156°. Different bars represent different transfer channels.

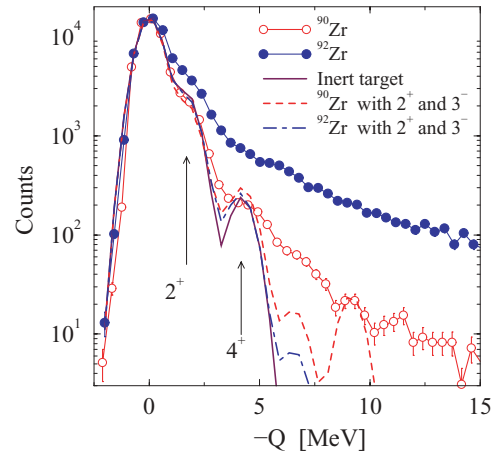

FIG. 5. (Color online) Inelastic (nontransfer) Q-value spectra for ^{20}Ne + ^{90,92}Zr (open and filled circles, respectively), taken from scattering of the ^{20}Ne projectile at 156°. The circles show the number of counts in a 0.44-MeV Q-value bin. Lines represent CC calculations after folding with the experimental resolution (see text). The solid line treats the zirconium targets as inert (i.e., it ignores their excitations), whereas the dashed line for ^{90}Zr and the dot-dashed curve for ^{92}Zr take into account the single and mutual excitations of the target quadrupole- and octupole-phonon states. All distributions are normalized to have the same value as the ^{20}Ne + ^{90}Zr data at the elastic peak.

^{20}Ne ions from both targets. The CM detector angle is 156° in both cases and the CM energy is 51.85 MeV. The solid curve shows the result of a CC calculation ignoring target excitations but including the 2^+ and 4^+ states in ^{20}Ne. [The inclusion of the 6^+ state gives no discernible difference on this scale, and the small target-radius difference (from the $A^{1/3}$ factor) also makes a negligible difference to the curve.] To make a meaningful comparison with the experimental data, this theoretical curve and subsequent calculations have been folded with a Gaussian $\exp(-Q^2/\Delta^2)$, with $\Delta = 0.75$ MeV, to simulate the detector resolution; this is seen to work well in the region of the elastic peak, where all of the curves displayed are normalized to have the same value as the ^{20}Ne + ^{90}Zr data.

We note that although the calculation fits the ^{90}Zr data extremely well up to around 5 MeV, it considerably underestimates the cross section for ^{92}Zr. The inclusion of the quadrupole- and octupole-phonon states in the targets does not resolve this discrepancy. The dashed curve for ^{90}Zr ($E_{2^+} = 2.18$ MeV, $\beta_2 = 0.10$; $E_{3^-} = 2.75$ MeV, $\beta_3 = 0.17$) shows an improvement of the fit, and it may even explain some of the higher energy structure in the data, but the dot-dashed curve for ^{92}Zr ($E_{2^+} = 0.93$ MeV, $\beta_2 = 0.10$; $E_{3^-} = 2.34$ MeV, $\beta_3 = 0.17$) does nothing to improve the large underestimate of the experimental data with that target.

In Fig. 6, we show the difference (squares) between the experimental data for the two systems, and we note that it possesses no oscillatory structure in the region of the energies of the 2^+ and 4^+ states in ^{20}Ne. We conclude, therefore, that, as predicted by the theoretical calculations, the contribution to the Q-value spectra from projectile excitations is the same in both reactions, and the difference must be due to a

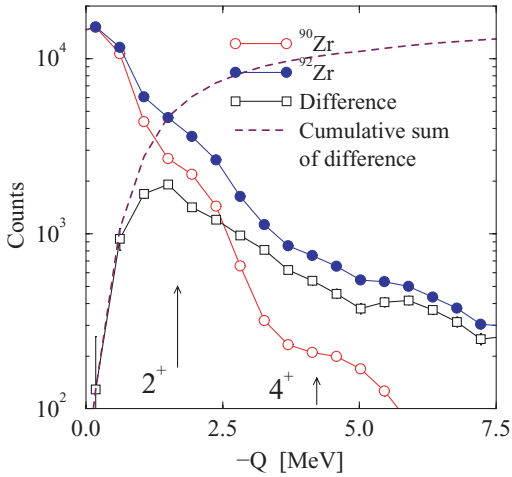

FIG. 6. (Color online) Squares show the difference between the ^{20}Ne + ^{92}Zr inelastic data (filled circles) and those for ^{20}Ne + ^{90}Zr (open circles). In the region between the energies of the 2^+ and 4^+ states in ^{20}Ne, the difference shows none of the structure due to the coupling to those states that is seen in the individual curves. This implies that their contributions are the same in both reactions. The cumulative sum of the difference (dashed line) shows that 75% of the extra cross section in the ^{20}Ne + ^{92}Zr reaction comes from the region $-Q < 5$ MeV.

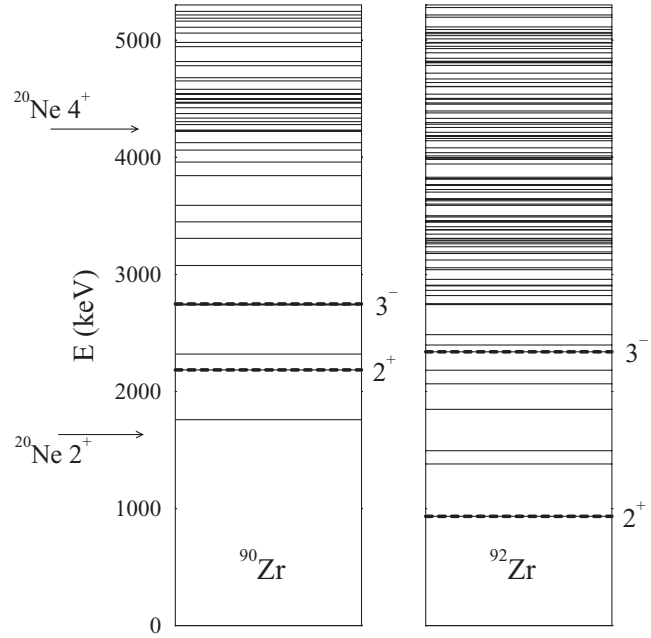

FIG. 7. Known levels in ^{90}Zr and ^{92}Zr up to 5.3 MeV [20]. The level density is significantly higher for the heavier isotope owing to the two valence neutrons outside the $N = 50$ closed shell. The dashed lines indicate the energies of the most collective states in these two nuclides; quadrupole (2^+) and octupole (3^-) vibrational states. Even these collective states individually contribute little to the Q-value spectra (see Fig. 5). It is clear, however, that the large number of noncollective (n-particle-n-hole) states generates a broad background to the Q-value spectrum for ^{20}Ne + ^{92}Zr. Arrows indicate the energies of the 2^+ and 4^+ rotational states in ^{20}Ne. Note that 75% of the noncollective background comes from states below 5 MeV excitation energy.

"background" of noncollective (n-particle-n-hole) excitations in ^{92}Zr, which possesses two valence neutrons outside the closed $N = 50$ neutron shell in ^{90}Zr. From the cumulative sum of this difference (dashed curve in Fig. 6), we see that 75% of the extra cross section for ^{92}Zr comes from contributions having $-Q < 5$ MeV. Furthermore, since the noncollective background for ^{90}Zr is very small (see Fig. 5), the total sum gives a good approximation for the differential cross section to the noncollective states in ^{92}Zr. We find a value of around 13 mb/ster at this scattering angle (156°). This is more than a factor of 3 larger than the contribution from transfer channels.

These observations can be understood in terms of the energy level diagrams for these two isotopes shown in Fig. 7 [20]. We also indicate in this figure the energies of the 2^+ and 4^+ states in ^{20}Ne and the energies of the quadrupole and octupole target states. We see that below the energy of the 4^+ state in ^{20}Ne, there are rather few noncollective states in ^{90}Zr, whereas there are very many in ^{92}Zr. The extra background in the latter case is, therefore, not surprising. Furthermore, we see that the collective states of the target, which are easy to take into account in the CC calculations, are embedded among the noncollective states. It is very difficult to account for these states in CC calculations for two reasons: 1. Their large number makes the calculations intractable and 2. there is, in any case, no simple description for the couplings to them.

We shall, therefore, treat the effect of the many noncollective states in the usual way, that is, using an imaginary component to the optical potential. This is nonetheless a significantly more complete description of the full problem than usual, since the collective excitations can still be treated through the CC approach. In the language of the "barrier distribution," the barriers can still be evaluated via CC calculations, but the elastic scattering from each barrier will be calculated using a standard optical-model potential. The imaginary part will clearly be small for ^{20}Ne + ^{90}Zr, but significantly larger for ^{20}Ne + ^{92}Zr. We shall see that the effect of this on the elastic test function of Eq. (3) for this system is responsible for the smearing of the quasielastic barrier distribution.

In fact, we will show that because the underlying barrier distributions for these two systems are the same, we can, in this special case, bypass the theoretical calculation of $D_{\rm QE}$ for ^{20}Ne + ^{92}Zr and reproduce the experimental data through a simple transformation of the data for ^{20}Ne + ^{90}Zr. This transformation will, of course, depend on the nature of the absorptive potential for ^{20}Ne + ^{92}Zr, which we shall now investigate.

III. BROADENING THE QUASIELASTIC PEAKS

We now wish to demonstrate that the broadening of the quasielastic test function of Eq. (3) (i.e., the single-barrier peak) is sufficient to explain the shape of the $D_{\rm QE}$ for the ^{92}Zr target. Clearly, these individual quasielastic peaks ($f_{\rm QE}$) will depend on the degree of absorption into the weak, direct-reaction channels, which is generally represented by the introduction of a surface imaginary potential in optical-model

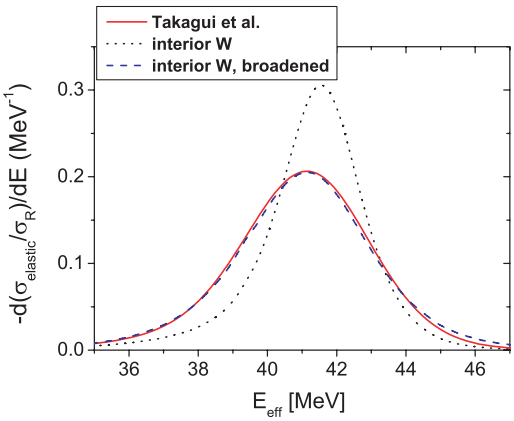

FIG. 8. (Color online) Test function for the one-channel calculation (^{16}O + ^{92}Zr) with the optical-model potential of Takagui *et al.* (solid line), the same with the imaginary potential confined to the nuclear interior (dotted line), and the result of transforming the latter $f_{\rm QE}$ to the wider one (dashed line). See text.

calculations. From the discussion of Fig. 5, it might be expected that $f_{\rm QE}$ for ^{90}Zr should be close to that for no surface absorption, whereas for ^{92}Zr it should be equivalent to significantly higher absorption.

Figure 8 (solid line) shows a calculation of the test function $f_{\rm QE} = -d(\sigma_{\rm elastic}/\sigma_R)/dE_{\rm eff}$. To avoid any *ad hoc* parameter fitting, we use the results of some independent optical-model calculations for the system ^{16}O + ^{92}Zr obtained by Takagui *et al.* [21] by fitting the angular distribution for elastic scattering at near-barrier energies. The potential has real parameters $U = 59.9$ MeV, $r_\circ = 1.2$ fm, and $a = 0.63$ fm and imaginary parameters $W = 131.3$ MeV, $r_\circ = 1.2$ fm, and $a = 0.42$ fm. Note that relating results from this potential to those in our system would not be legitimate if transfers were important, because these channels would clearly be different with the ^{20}Ne projectile. Furthermore, it is important that the imaginary potential that we are taking from the ^{16}O + ^{92}Zr system does not contain a significant contribution from collective excitations of the ^{16}O projectile. This is a reasonable approximation, because the lowest collective state in that nuclide is the very high lying octupole-phonon state at 6.13 MeV.

Figure 8 also shows (dotted line) the $f_{\rm QE}$ calculated without surface absorption (i.e., with an imaginary potential confined to the nuclear interior; $W = 30$ MeV, $r_\circ = 0.9$ fm, and $a = 0.3$ fm). This turns out to be significantly sharper; the difference is due to absorption corresponding to inelastic excitations in ^{92}Zr. The transformation of the narrow test function into the wider one can be easily simulated, for example, by a Gaussian convolution [$\exp(-x^2/\Delta^2)$ with $\Delta = 1.65$ MeV] and a small energy shift of -0.31 MeV (see Fig. 8).

Because Eq. (3) is a simple sum of single-channel test functions, the same transformation can be applied to the full distribution $D_{\rm QE}$, and it should transform the experimental barrier distribution for ^{20}Ne + ^{90}Zr into that for ^{20}Ne + ^{92}Zr, with no further theoretical input. This is confirmed by the resulting solid line shown in Fig. 2(b), which displays excellent agreement with the ^{92}Zr data. (Note, however, that in this case, where we are relating results in two different systems, we require a slightly different shift of -0.50 MeV in the described transformation. This can easily be understood in terms of the marginally different barrier heights in the two cases, arising simply because the radius of ^{92}Zr is around 0.04 fm larger than that of ^{90}Zr.) We see then, from Fig. 2, that it is merely the effect of the broader test function for ^{92}Zr that blurs the structure present in the ^{90}Zr data, even though the underlying barrier distributions (defined by w_i and B_i) are essentially the same in both cases. In other words, the weak couplings reduce the resolving power of the quasielastic method and lead to a smeared barrier distribution.

We emphasize that the present systems are special; their interpretation is rather unambiguous because the two underlying barrier distributions, both dominated by the ^{20}Ne deformation, are the same because both targets have the same charge, $Z = 40$. The only remaining isotopic dependence is then in the weakly coupled reaction channels, which, as we have shown, determine the width of the individual components of the distribution. Of course, the weak channels are significantly more numerous in ^{92}Zr than in ^{90}Zr (see Fig. 8), owing to the closed neutron shell in the latter isotope.

Such effects will also play a role in the systems that we previously studied (^{20}Ne + $^{\rm nat}$Ni, where structure is observed [22], and ^{20}Ne + ^{118}Sn, where it is not [23]), although in these cases, the isotopic dependence, which allows us to draw very definite conclusions in the present case, has not been investigated.

The smoothing concept may be further tested experimentally, because, in principle, fusion is much less sensitive to weakly coupled channels. Indeed, some evidence for this already exists in the ^{16}O + ^{144}Sm system [4,7] that has already been mentioned. In this case, a clearly resolved peak in $D_{\rm fus}$ simply becomes a broad shoulder in $D_{\rm QE}$. We should equally expect the structure observed in $D_{\rm QE}$ for ^{20}Ne + ^{90}Zr to show up in $D_{\rm fus}$ for ^{20}Ne + ^{92}Zr, even though it is absent from its quasielastic distribution.

It should be noted that this proposed mechanism is different from that proposed for the smoothing of the so-called elastic barrier distribution in Ref. [24]. In that case, the total elastic amplitude may be thought of as arising from a weighted sum of the elastic-scattering *amplitudes* from the different barriers. Although each of these amplitudes will still be smeared by coupling to weak channels, they will also each have a different overall phase, leading to a "dephasing" of the total amplitude and a further loss of structure in the total elastic barrier distribution. The present case is, however, much clearer because the quasielastic cross section is the *incoherent* sum of elastic *cross sections* from each barrier, and the smoothing of the overall distribution can arise only from a smoothing of the individual contributions to it.

IV. CONCLUSIONS

In conclusion, we have shown that QE barrier distributions can be smoothed by scattering into a large number of weak (noncollective) excitations. Moreover, it appears possible to

treat these and the few strongly coupled, collective channels simultaneously in a simple way. The strong channels appear to determine the underlying barrier distribution, whereas the weak channels smear the peak from each individual barrier, an effect that is reflected in calculations using a standard optical-model imaginary potential. Although the possible effects of transfer channels have frequently been investigated, we believe that this is the first time that the effects of noncollective inelastic channels have been explicitly brought to light.

The possibility of including a large number of weak channels explicitly in CC calculations is currently being pursued [25]. In a preliminary one-dimensional model, using random-matrix theory [26] to generate the many noncollective couplings [27], the conjecture of an underlying distribution generated by the collective channels and smeared by the weak channels appears to be borne out. The same model can also be applied to generate an optical potential that takes into account the noncollective excitations [26,28], and it will be interesting to see how such an optical potential leads to a smeared barrier distribution.

ACKNOWLEDGMENTS

We are grateful to the Warsaw Cyclotron staff for the excellent beam they provided. We thank L. Pieńkowski for assisting in data analysis and also the target production staff of the LNL, in particular M. Loriggiola. This work was funded in part by Grant No. N202 152 31/2796 and supported by the cooperation agreement (03-110) between the IN2P3 (France) and the Polish laboratories.

[1] M. Dasgupta *et al.*, Annu. Rev. Nucl. Part. Sci. **48**, 401 (1998).
[2] As demonstrated by the wide variety of domains covered in Proceedings of the 4th International Symposium on "Foundations of Quantum Mechanics," Tokyo, 1992, JJAP Series 9 (1993).
[3] N. Rowley, G. R. Satchler, and P. H. Stelson, Phys. Lett. **B254**, 25 (1991).
[4] H. Timmers *et al.*, Nucl. Phys. **A584**, 190 (1995).
[5] L. F. Canto *et al.*, Phys. Rep. **424**, 1 (2006).
[6] K. Hagino and N. Rowley, Phys. Rev. C **69**, 054610 (2004).
[7] F. M. Zamrun and K. Hagino, Phys. Rev. C **77**, 014606 (2008).
[8] V. I. Zagrebaev, Phys. Rev. C **78**, 047602 (2008).
[9] H. Timmers *et al.*, Nucl. Phys. **A633**, 421 (1998).
[10] M. A. Nagarajan, A. B. Balantekin, and N. Takigawa, Phys. Rev. C **34**, 894 (1986).
[11] S. Raman, C. W. Nestor Jr., and P. Tikkanen, At. Data Nucl. Data Tables **78**, 1 (2001); T. Kibedi and R. H. Spear, At. Data Nucl. Data Tables **80**, 35 (2002).
[12] E. Piasecki *et al.*, Int. J. Mod. Phys. E **16**, 502 (2007).
[13] E. Piasecki *et al.*, Phys. Rev. C **65**, 054611 (2002).
[14] K. Hagino and N. Rowley (unpublished).
[15] I. I. Gontchar, D. J. Hinde, M. Dasgupta, C. R. Morton, and J. O. Newton, Phys. Rev. C **73**, 034610 (2006).
[16] A. M. Stefanini, J. Phys. G **23**, 1401 (1997); G. Montagnoli *et al.*, Eur. Phys. J. A **15**, 351 (2002); G. Pollarolo and A. Winther, Phys. Rev. C **62**, 054611 (2000).
[17] A. M. Stefanini *et al.*, Phys. Rev. C **73**, 034606 (2006).
[18] E. Piasecki *et al.*, AIP Conf. Proc. **1012**, 238 (2008).
[19] G. Pollarolo, Phys. Rev. Lett. **100**, 252701 (2008).
[20] Brookhaven National Laboratory, Evaluated Nuclear Structure Data File, http://www.nndc.bnl.gov/ensdf/. See references therein.
[21] E. M. Takagui *et al.*, Nucl. Phys. **A514**, 120 (1990).
[22] Ł. Świderski *et al.*, Int. J. Mod. Phys. E **14**, 341 (2005).
[23] Ł. Świderski *et al.*, Int. J. Mod. Phys. E **13**, 315 (2004); E. Piasecki, Phys. Lett. **B615**, 55 (2005).
[24] N. Rowley *et al.*, Phys. Lett. **B373**, 23 (1996).
[25] K. Hagino, S. Yusa, and N. Rowley (to be published).
[26] D. Agassi, C. M. Ko, and H. A. Weidenmüller, Ann. Phys. (NY) **107**, 140 (1977).
[27] M. C. Nemes, Nucl. Phys. **A315**, 457 (1979).
[28] B. V. Carlson, M. C. Nemes, and M. S. Hussein, Phys. Lett. **B91**, 332 (1980).